of holes allows the magnetic breakdown that has been observed in several experiments.[7-9] Since all of the data recorded here were obtained in magnetic fields less than 1 kG, no breakdown effects were observed.

The curve labeled G in Fig. 2 is assigned to the portion of the third band of electrons occurring on the Brillouin zone boundary (stars). The peaks recorded on curve G are an order of magnitude less intense than the other observed peaks and become obscured for caliper dimensions of the same size as those arising from the first and second bands. The free-electron construction indicates that the calipers obtained from this sheet of the Fermi surface should trace out an ellipse for field rotations in the basal plane. The data, however, show a distortion from this picture, with the expected elliptical shape being squeezed into an elongated cigar shape.

There are four remaining curves, H, I, J, and K, which we have been unable to assign to orbits on the various sheets of the Fermi surface predicted by the free-electron construction. Curve H has the same angular dependence for both its caliper size and its intensity as the minimum open orbit and remains an almost constant value of k_c smaller than the calipers for this orbit for all angles. Curves I, J, and K are of low

intensity. All of the k_c values obtained in these remaining curves are too large to agree with the expected sizes of the fourth-band holes (cigars). The fact that no size-effect peaks are observed, which can be attributed to the fourth-band cigars, by no means precludes their existence. In the field ranges that they are expected to occur, the surface impedance changes rapidly and they may be lost in the background.

A direct comparison of the results of this experiment to calipers obtained by ultrasonic geometric resonance can only be made for the third-band lens and the first-band caps. The various values for the diameter of the lens in the basal plane are tabulated in Table I. The [$11\bar{2}0$] caliper assigned to the caps in the present experiment is 0.300 Å^{-1}. This is in excellent agreement with the value of 0.295 Å^{-1} obtained by Chang[4] for this direction. Gibbons and Falicov[2] have assigned a caliper of 0.31 Å^{-1} for the [$11\bar{2}0$] direction to the second band at the AHL plane. This particular caliper cannot be obtained directly from the present results, but it is in agreement with the first-band caliper for this direction, since the energy gap between the first and second bands is small in this direction.

ACKNOWLEDGMENT

[8] A. D. C. Grassie, Phil. Mag. **9**, 847 (1964).
[9] J. K. Galt, F. R. Merritt, and J. N. Klauder, Phys. Rev. **139**, A823 (1965).

Fermi Surface of Magnesium. I. Magnetoacoustic Attenuation*

J. B. Ketterson
Argonne National Laboratory, Argonne, Illinois

AND

R. W. Stark†
*Department of Physics and Institute for the Study of Metals
The University of Chicago, Chicago, Illinois*

(Received 21 October 1966)

Geometric resonances in the ultrasonic attenuation have been studied in magnesium for sound propagated in the three principle crystallographic directions. A total of twenty different geometric resonance branches have been obtained. The assignment of these branches to Fermi-surface calipers shows that the magnesium Fermi surface is much more free-electron-like than currently thought. Three of the first four local pseudopotential Fourier expansion coefficients are estimated from data to be 5×10^{-4} 1.0×10^{-2}, and 1.7×10^{-2} Ry for the absolute value of the [$10\bar{1}0$], [0002], and [$10\bar{1}1$] coefficients, respectively. A two orthogonalized-plane-wave model is given for the lens-shaped piece of the Fermi surface in the third Brillouin zone, and various physical properties of this model are calculated and compared with experimental data.

I. INTRODUCTION

THE Fermi surface of magnesium has been the subject of several experimental and theoretical investigations during the past few years. The anoma-

lous skin effect[1] has yielded a value for the total area of the Fermi surface; the de Haas–van Alphen effect[2-5]

[1] E. Fawcett, J. Phys. Chem. Solids **4**, 320 (1961).
[2] W. L. Gordon, A. S. Joseph, and T. G. Eck, in *The Fermi Surface*, edited by W. A. Harrison and M. B. Webb (John Wiley & Sons, Inc., New York, 1960), p. 84.
[3] M. G. Priestley, Proc. Roy. Soc. (London) **A276**, 258 (1963).
[4] M. G. Priestley, L. M. Falicov, and Gideon Weisz, Phys. Rev. **131**, 617 (1963).
[5] R. W. Stark, Bull. Am. Phys. Soc. **11**, 169 (1966); (to be published).

has been used to measure several of its extremal cross-sectional areas; cyclotron resonance[6,7] has given values for the cyclotron mass of various orbits on the surface; and the galvanomagnetic properties[8-10] have yielded information about its topology. All of these experiments have been shown to be in *reasonable* agreement with a Fermi-surface model based on Falicov's orthogonalized-plane-wave (OPW) band-structure calculations.[11]

The present contribution describes the results of extensive magnetoacoustic measurements in magnesium.[12] The objective of this work is to gain a better understanding of the magnesium Fermi surface.

II. THE MAGNESIUM LATTICE

The real-space lattice of hexagonal-close-packed (hcp) magnesium is shown in Fig. 1. This is defined by a right-handed system of three primitive translation vectors t_1, t_2, and t_3, the angle between t_1 and t_2 or t_3 being 90°, and the angle between t_2 and t_3 being 120° with

$$|t_1| = c,$$
$$|t_2| = |t_3| = a. \tag{1}$$

There are two atoms per unit cell of the hcp structure, located at the origin and τ, respectively, where

$$\tau = \tfrac{1}{2}t_1 + \tfrac{1}{3}t_2 + \tfrac{2}{3}t_3. \tag{2}$$

The volume V of this unit cell is

$$V = t_1 \cdot t_2 \times t_3 = a^2 c \sin(2\pi/3). \tag{3}$$

The lattice parameters measured at 293°K and extrapolated to 0°K using the thermal-expansion data of McCammon and White[13] are listed in Table I together with other information pertinent to the crystal structure.

The reciprocal lattice is defined by the three vectors G_1, G_2, and G_3, related to the real-space vectors by

$$G_i = 2\pi t_j \times t_k / t_i \cdot t_j \times t_k, \tag{4}$$

$i, j, k = 1, 2, 3$ in cyclical order.

Thus,

$$|G_1| = 2\pi/c,$$
$$|G_2| = |G_3| = 2\pi/a \sin(2\pi/3). \tag{5}$$

The first Brillouin zone of the hcp structure is shown

[6] T. G. Eck and M. P. Shaw, in *Proceedings of the IXth International Conference on Low-Temperature Physics, Columbus, Ohio, 1964* (Plenum Press, Inc., New York, 1965), p. 759.

[7] D. M. Zych, Ph.D. thesis, Case Institute of Technology (unpublished); D. M. Zych and T. G. Eck (to be published).

[8] R. W. Stark, T. G. Eck, W. L. Gordon, and F. Moazed, Phys. Rev. Letters **8**, 360 (1962).

[9] R. W. Stark, T. G. Eck, and W. L. Gordon, Phys. Rev. **133**, A443 (1964).

[10] R. W. Stark (to be published).

[11] L. M. Falicov, Phil. Trans. Roy. Soc. (London) **A255**, 55 (1962).

[12] J. B. Ketterson and R. W. Stark, Bull. Am. Phys. Soc. **11**, 90 (1966).

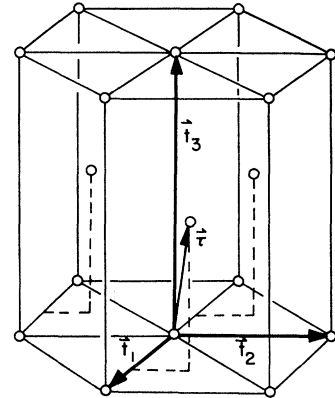[13] R. D. McCammon and G. K. White, Phil. Mag. **11**, 1125 (1965).

FIG. 1. The hexagonal-close-packed lattice structure. t_1, t_2, and t_3 are the primitive translation vectors. There are two atoms per unit cell centered at the origin and τ.

in Fig. 2 together with various points and lines of symmetry. The volume Ω, enclosed by this zone, is

$$\Omega = G_1 \cdot G_2 \times G_3 = (2\pi)^3 / V. \tag{6}$$

Each zone contains a number of states sufficient to hold two electrons for each unit cell of the crystal.

III. BAND-STRUCTURE THEORY

Atomic magnesium has the electronic configuration $1s^2 2s^2 2p^6 3s^2$. In the solid state the two $3s$ electrons are contributed to the conduction band leaving the magnesium core in the tightly bound neon-like configuration. Since there are two atoms per unit cell of the hcp lattice, a total of four electrons are contributed to the conduction band for each unit cell of the crystal. This just fills a volume of states in reciprocal space equal to twice the volume Ω.

The wave functions of the conduction electrons in the crystal show little resemblance to the $3S$ wave functions for the free atom. The Schrödinger equation for the crystal,

$$[(-\hbar^2/2m)\nabla^2 + V(\mathbf{r})]\psi = E\psi, \tag{7}$$

TABLE I. Physical constants for magnesium (in atomic units).

Real-space lattice:	
$t_1(300°K) = 9.8461$	$t_2(300°K) = t_3(300°K) = 6.0645$
$t_1(0°K) = 9.7811$	$t_2(0°K) = t_3(0°K) = 6.0260$
$V(0°K) = 307.62$	
Reciprocal lattice:	
$G_1(0°K) = 0.6424$	$G_2(0°K) = G_3(0°K) = 1.2039$
$\Omega = 0.8063$	
Free-electron Fermi sphere:	
$k_F = 0.7275$	$E_F = k_F^2 = 0.5292$
Density:	
$\rho = 1.738$ g/cm³	
Elastic constants:	
$c_{11} = 6.322 \times 10^{11}$ g/cm-sec²	
$c_{33} = 6.561 \times 10^{11}$ g/cm-sec²	
Longitudinal sound velocity:	
$V_{\text{BASAL}} = 6.036 \times 10^5$ cm/sec	$V_{0001} = 6.144 \times 10^5$ cm/sec
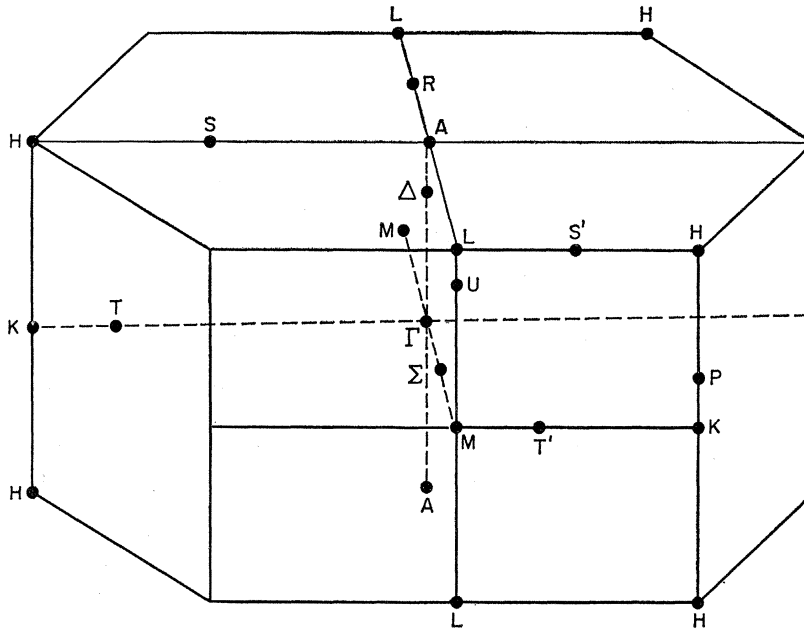
FIG. 2. The first Brillouin zone for the hexagonal-close-packed structure. The ΓA, ΓM, and ΓK directions correspond to the [0001], [10$\bar{1}$0], and [11$\bar{2}$0] crystallographic directions, respectively. ΓA is along G_1 and ΓM is along G_2 or G_3.

must be solved. The conduction-electron wave functions ψ are now Bloch states and $V(r)$ is the periodic potential due to the ion cores and the self-consistent field of all electrons. $V(r)$ is a rapidly varying function with a strong attractive part close to the ion cores. The conduction states ψ must be orthogonal to the core states ψ_c. This constraint forces the conduction electrons to sample $V(r)$ in a very special way which can be represented by a new wave equation which is identical to Eq. (7) but with an effective or pseudopotential $U(r)$ (replacing $V(r)$) which is both much weaker than $V(r)$ and more smoothly varying,[14] and a new wave function φ which is much smoother than ψ. In practice $U(r)$ may be represented by a Fourier expansion

$$U(r) = \sum_{G_i} V_{G_i} e^{iG_i \cdot r}, \qquad (8)$$

where the V_{G_i} in general are momentum-dependent. In the local approximation these are treated as momentum-independent. In either case, the Fourier expansion generally converges sufficiently rapidly so that the series can be truncated after a few terms. In fact, a reasonable first approximation to the electronic band structure of magnesium is obtained by keeping only the leading constant term $U(r) = V_0$. This results in spherical constant-energy surfaces centered on Γ. The radius k_F of the spherical surface at the Fermi energy is $k_F = (3\Omega/2\pi)^{1/3}$. The higher-order terms in the expansion, though small, are of essential importance in determining the electron dynamics and the actual form of the Fermi surface. The idealized single-OPW model proposed by Harrison[15] truncates the series to its leading

term but constrains the electrons motion to a single zone.

Since the magnesium lattice contains two atoms per unit cell, the V_{G_i} contain contributions from the ion core potentials v_{G_i} of the individual atoms. The contribution from each of these cores must be added with the proper phase. This can be written in the form $V_{G_i} = S(G_i) v_{G_i}$, where $S(G_i)$ is the structure factor for magnesium,

$$S(G_i) = 1 + \exp(iG_i \cdot \tau). \qquad (9)$$

It should be noted that $S(G_i)$ is identically zero for $G_i = G_1$. This is a property common to all hcp metals. For the position-dependent potential $V(r)$ used in Eq. (7) this leads directly to a vanishing of the energy discontinuity across the AHL plane of the Brillouin zone shown in Fig. 2.[16] However, a more general treatment including spin-dependent terms,[17] in particular spin-orbit coupling, yields a discontinuity across the AHL plane except along the AL line. In magnesium (because of its low atomic number) the maximum value of this discontinuity is expected to be about 5×10^{-4} Ry. This is so small that one must consider the probability that magnetic breakdown[18-20] may be important in magnetic fields as small as a few hundred gauss. The measurements reported in this paper were made in

[14] W. A. Harrison, *Psuedopotentials in the Theory of Metals* (W. A. Benjamin, Inc., New York, 1966) and references therein.
[15] W. A. Harrison, Phys. Rev. **118**, 1182 (1960).

[16] N. F. Mott and H. Jones, *The Theory of the Properties of Metals and Alloys* (Dover Publications, Inc., New York, 1958), p. 161.
[17] M. H. Cohen and L. M. Falicov, Phys. Rev. Letters **5**, 544 (1960); L. M. Falicov and M. H. Cohen, Phys. Rev. **130**, 92 (1963).
[18] M. H. Cohen and L. M. Falicov, Phys. Rev. Letters **7**, 231 (1961).
[19] E. I. Blount, Phys. Rev. **126**, 1636 (1962).
[20] A. B. Pippard, Proc. Roy. Soc. (London) **A270**, 1 (1962); Phil. Trans. Roy. Soc. (London) **256**, 317 (1964).
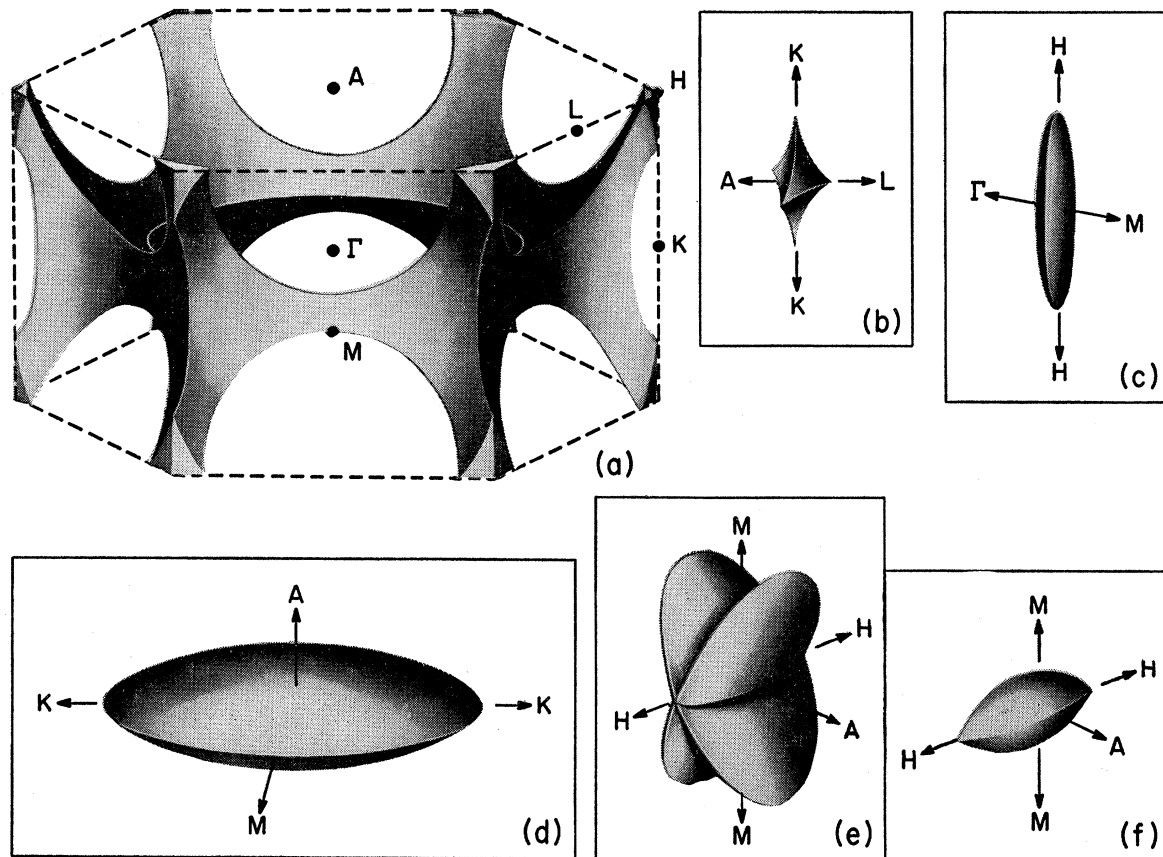
Fig. 3. The single-OPW model Fermi surface for magnesium: (a) monster (2nd-zone holes); (b) cap (1st-zone holes); (c) cigar (3rd-zone electrons); (d) lens (3rd-zone electrons); (e) butterfly (3rd-zone electrons); (f) fourth-zone electrons.

magnetic fields of less than 300 G and in this range of fields we found that the Brillouin zone shown in Fig. 1 was appropriate for the description of the band structure.

The single-OPW model has sheets in the first four zones. These are shown in the *reduced* zone scheme in Fig. 3(a)–3(f) and are described below in order of increasing zone number.

Caps: Two identical hole pockets in the first zone centered around H. Their shape is approximately that of two regular tetrahedrons set base to base. [Fig. 3(b)].

Monster: A multiply-connected hole surface in the second zone centered on Γ. This sheet is capable of supporting a band of open trajectories parallel to G_1 (the ΓA direction) in low magnetic fields [Fig. 3(a)].

Cigars: Two identical electron pockets in the third zone centered around K. The cross sections of these pieces in the ΓKM plane is very nearly that of an equilateral triangle [Fig. 3(c)].

Lens: A large electron pocket in the third zone centered on Γ which has the shape of a convex lens [Fig. 3(d)].

Butterflies: Three identical electron pockets in the third zone centered on L. These have the shape of two

intersecting convex lenses tilted at an angle of approximately 57° with respect to one another [Fig. 3(e)].

Fourth-zone electron pockets: Three identical electron pockets centered on L in the fourth zone. The cross section of these pieces in the LAM plane is approximately that of an equilateral parallelogram with an enclosed angle of about 57° at the vertex toward M. These sheets do not have a conventionally accepted colloquial name [Fig. 3(f)].

At this time no reasonable doubt remains as to the existence of all of these pieces of the Fermi surface of magnesium. Previously reported de Haas–van Alphen measurements have verified their presence; galvanomagnetic measurements have verified their general topology.

Falicov[11] has carried out a careful OPW calculation from first principles for the band structure of magnesium. His results yield all of the pieces described above for the single-OPW model. The relative shapes of his pieces agree with the single-OPW model but their dimensions are generally somewhat smaller. A comparison of our experimentally determined dimensions with both the single-OPW model and Falicov's model will be made later in this paper. (see Table II).

IV. ULTRASONIC-ATTENUATION THEORY

In the standard geometry used for studying geometric resonances in the ultrasonic attenuation of a metal, the magnetic field **H** is constrained to move in the plane perpendicular to the sound propagation direction **q**. With this geometry, a simple expression relates the frequency F of a geometric resonance to an extremal Fermi surface caliper k_{ext} by[21,22]

$$F = (\hbar c/e\lambda)k_{ext}, \qquad (10)$$

where λ is the sound wavelength and e, h, and c have their usual significance. k_{ext} measures the extremal projection of the Fermi surface in the direction perpendicular to both **H** and **q**, i.e., in the direction of the unit vector

$$\hat{u} = \hat{q} \times \hat{H}. \qquad (11)$$

In principle, these extremals are determined by examining the projection of orbits in reciprocal space upon $\hat{u}$ for a continuous series of parallel-orbit planes separated by an amount $d\mathbf{k}_H$, where $\mathbf{k}_H$ is measured parallel to **H**. When such a projection passes through an extremal as a function of $\mathbf{k}_H$, a geometric resonance may be observed. In general these extremal calipers can not be uniquely converted into radius dimensions of the Fermi surface. However, this conversion is unique if a given Fermi surface sheet has sufficient symmetry so that a set of extremal calipers measured on it for different directions of **H** all occur in a common plane about a common center. This happens, in particular, if a given sheet of the Fermi surface has both reflection symmetry in a plane perpendicular to **q** and inversion symmetry about some point in that plane.

Throughout this paper we will use the following system of notation. If the Fermi surface sheet in question has sufficient symmetry, we will reduce the

measured calipers to radii. These reduced radii will be referred to by the symbol k, generally including a subscript name identifying the orbit calipered and a superscript indicating the direction of the caliper with respect to the Brillouin zone shown in Fig. 2. For example, $k_{LENS}^{\Gamma K}$ refers to the radius of the lens measured from Γ toward K. Calipers associated with orbits having insufficient symmetry to allow a direct conversion into Fermi surface radii will be denoted by the symbol C which will also carry equivalent superscripts and subscripts.

To observe geometric resonance the electron-mean-free path l must be much larger than λ, i.e., $ql \gg 1$. l is generally determined by impurity scattering, phonon scattering, and surface scattering. At low fields the resonances begin when the electron completes approximately one orbit before scattering. If l is limited primarily by the geometrical size of the crystal, the resonances begin when the orbit size is smaller than the shortest crystal dimension in the plane of the orbit (usually the propagation direction). In either case, the resonances cease at high fields when the orbit size becomes comparable to λ.

Since the sound waves constitute probes of finite dimensions, the resonance condition specified by Eq. (10) will not necessarily be valid in fields sufficiently high that the extremal orbit dimension is only a few sound wavelengths (low-phase region). In this case λ is a significant fraction of the orbit diameter and the phase of the oscillation shifts from its low-field asymptotic value. Thus, the oscillations are no longer strictly periodic in H^{-1}. In addition, a larger fraction of neighboring orbits with slightly different values of $\mathbf{k}_H$ may distort the phase in this region. In much lower fields where the extremal dimension is much larger than λ (high-phase region), we expect Eq. (10) to be rigorously satisfied and the resonances to be strictly periodic in
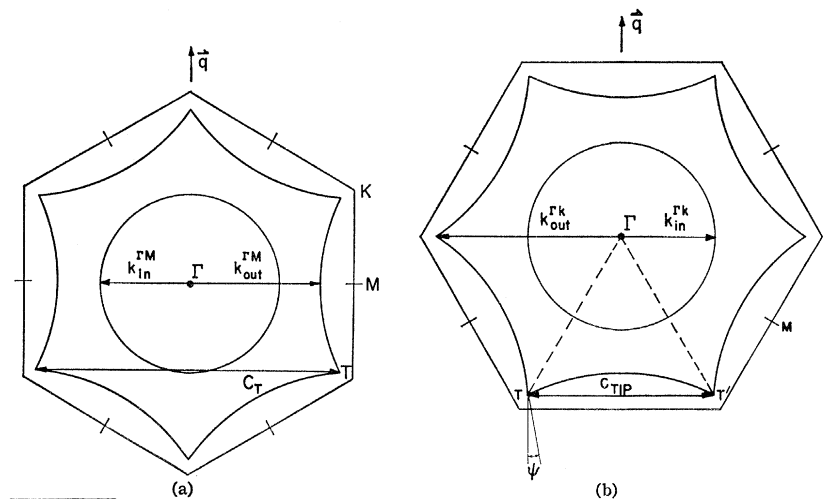

(a)   (b)

FIG. 4. Cross section of the monster in the ΓKM plane showing the extremal calipers on the orbits which may give rise to observable geometric resonances for **q** parallel to (a) $[11\bar{2}0]$ and (b) $[10\bar{1}0]$.

[21] M. H. Cohen, M. J. Harrison, and W. A. Harrison, Phys. Rev. **117**, 937 (1960).
[22] A. B. Pippard, Proc. Roy. Soc. (London) **A257**, 165 (1960).

H^{-1}. Deviations which may occur in the low-phase region are thus easily detected.

A given orbit may have more than one extremal caliper associated with it if it has more than one turning point. For example, consider the hexagonal-shaped orbit which occurs in the ΓKM plane of the monster. This is shown in Fig. 4(a) for $\mathbf{q}$ parallel to [11$\bar{2}$0]. It has been shown[23] that we may expect geometric resonances associated with the calipers $k_{\text{ext}} = C_T$, $2k_{\text{OUT}}{}^{\Gamma M}$, $C_T/2 \pm k_{\text{OUT}}{}^{\Gamma M}$.

The question naturally arises as to the relative amplitudes of these and other calipers. Intuitively we expect that if the electron spends a reasonably large fraction of a cyclotron period $2\pi/\omega_c$ at a turning point, the amplitude will be large. The exact theory[23] bears this out and shows that there is a factor $(\rho_a \rho_b)^{1/2}/v_a v_b m^{*2}$ in the amplitude, where ρ_a and ρ_b are the radii of curvature of the orbit at the turning points a and b, v_a and v_b are the velocities at the turning point (i.e., normal to the wavefront) and m^* is the effective mass of the electron on this orbit. In addition, we expect the amplitude to depend on the rate of change of the caliper as we move along $\mathbf{k}_H$ away from the extremal plane; the amplitude being smaller the more rapid this rate of change. Again, this is born out by the exact theory which contains a factor $(\partial^2 C/\partial k_H{}^2)^{-1/2}$, where C is the *nonextremal* caliper dimension as a function $\mathbf{k}_H$ and the expression is evaluated in the plane of the extremal orbit where $C = C_{\text{ext}}$. In a later section of this paper we will use a two-OPW approximation to evaluate these amplitude factors for orbits on the lens.

We now examine the monster in the ΓKM plane with $\mathbf{q}$ parallel [10$\bar{1}$0] as shown in Fig. 4(b). In this case we note that the point T near the tip of the arrow denoting C_{TIP} is not in reality a turning point on the orbit. As it happens, however, the motion of an electron on the segment of the orbit near this point is very nearly parallel to the sound wave front. The electron changes direction abruptly at T and then moves approximately perpendicular to the wave front. This introduces a cutoff in the electron-phonon energy-exchange integral and we expect an uncanceled energy exchange on a length Δk of the orbit near T given by $\Delta k = eH\lambda/2hc \sin\psi$, where ψ is the angle between the tangent line of the orbit at T and the sound wave front. This will contribute a geometric resonance of frequency $(hc/e\lambda)C_{\text{TIP}}$. We then expect to find geometric resonances arising from the calipers $2k_{\text{OUT}}{}^{\Gamma K}$, C_{TIP}, and $k_{\text{OUT}}{}^{\Gamma K} \pm C_{\text{TIP}}/2$.

Geometric resonances associated with nonextremal calipers may also be produced by another type of cutoff. In this case the cutoff is not in the energy-exchange integral as discussed above but is in the phase integral along $\mathbf{k}_H$. For example, consider the orbits on the butterfly for $\mathbf{H}$ parallel to [0001] and $\mathbf{q}$ parallel to [11$\bar{2}$0]. These are shown for the single-OPW model in

Fig. 5(b) for a series of planes cut perpendicular to $\mathbf{k}_H$. Notice that a saddle point occurs at $k_H = 0.09$ a.u. (k_H is measured with respect to L). After the saddle point (SP) the projection of the orbits along $\mathbf{u}$ changes abruptly to one-half the value before the saddle point (shown in Fig. 5). Thus the phase integral will yield uncanceled contributions both above and below the saddle point. We expect a contribution above the saddle point for approximately the distance $\Delta k_H = eH\lambda/2hc \tan\omega$, where ω is the angle between the tangent line to the butterfly in the ΓMLA plane at $k_H = 0.09$ a.u., and the ΓA direction. The resulting geometric resonance will measure the caliper C_{SP} shown in Fig. 5(b).

V. EXPERIMENTAL TECHNIQUES

The high-purity single crystals of magnesium which were used in this investigation were grown directly from the vapor phase in a special high-vacuum furnace. The details of this technique will be reported elsewhere.[24] The residual resistance ratio of these crystals was greater than 250 000.

Several samples with cross sectional areas and thicknesses of approximately 20 mm² and 2–3 mm, respectively, were prepared for directions of $\mathbf{q}$ parallel to the [0001], [10$\bar{1}$0], and [11$\bar{2}$0] crystallographic directions. The crystals were normally oriented to within 0.5° of a given crystallographic axis using standard x-ray techniques. The samples were cut to size with an acid string saw using a 12.5% aqueous solution of HCl and then the appropriate sides were planed parallel with a Servomet spark planer. The [0001] and [10$\bar{1}$0] samples were planed to within 0.1° of their respective crystallographic planes utilizing the natural crystalline faces which resulted as these crystals were grown.
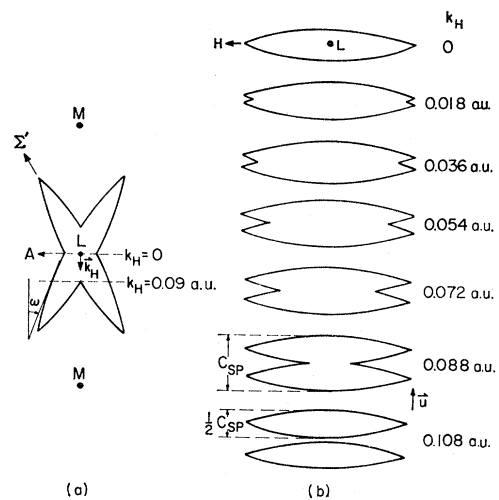

(a)   (b)

FIG. 5. (a) Cross section of the butterfly in the LAM plane showing the location of the saddle-point along the LM line at $k_H = 0.090$ a.u. (b) Cross sections of the butterfly normal to the LM line for various values of k_H.

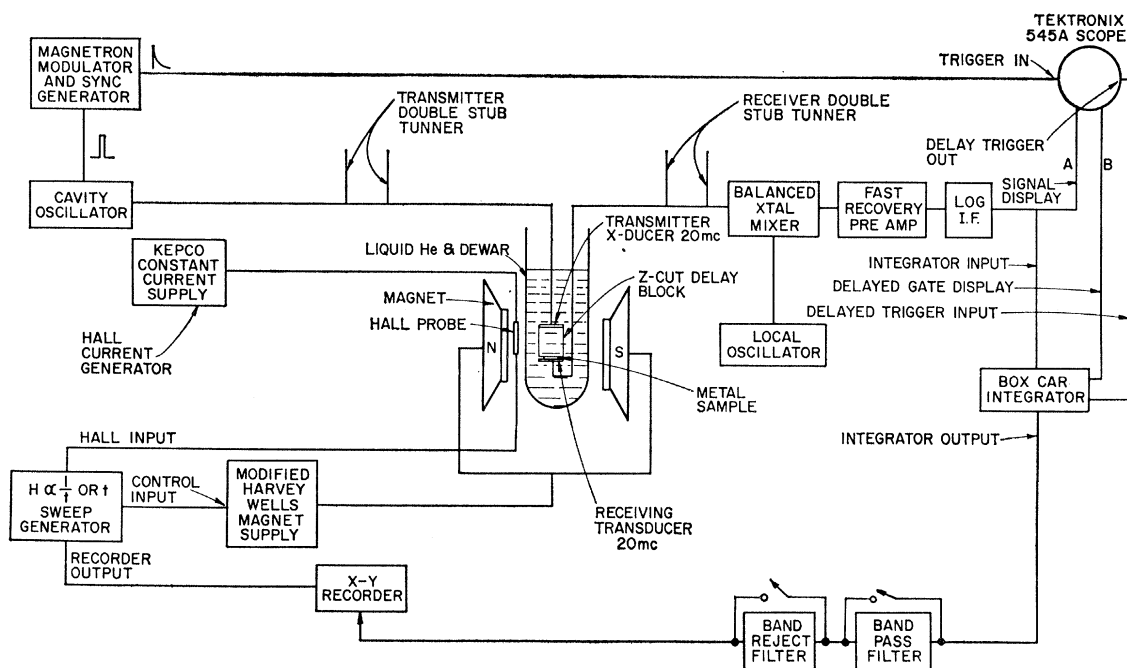[23] S. G. Eckstein (to be published).

[24] R. W. Stark (to be published).

FIG. 6. Block diagram of the experimental apparatus.

The planing surface of the Servo-met planer was replaced by a surface having $\frac{1}{16}$-in. wide grooves instead of the original $\frac{1}{4}$-in. wide grooves. The reason for this was simply that the sample dimensions were usually slightly smaller than $\frac{1}{4}$ in. and the results of planing with the original planing surface were quite unsatisfactory. The surfaces obtained were neither parallel nor unstrained. Satisfactory results were obtained with the $\frac{1}{16}$-in. wide grooves.

In order to observe the geometric resonance signals over a sufficient field range to get an accurate determination of their frequency, it was found to be necessary to restrict the sample thickness to 2–3 mm. This was the result of an unusually high nonresonant monotonic background attenuation which increased rapidly as the strength of the magnetic field was increased. This background became so large that no echoes were transmitted through these thin specimens when the magnetic field strength was raised to approximately 500 G.

An acoustic delay line (Z-cut quartz) was used to delay the transmitted pulse for a time sufficient to allow the cessation of the original pulse, since this was found to couple capacitively to the receiver. Coaxially plated x-cut transducers were used to generate and receive longitudinal sound waves. These were bonded to the crystal with Dow Corning No. 200 silicon fluid of viscosity 2×10^6 cP. The mounting geometry is shown in Fig. 6.

The upper curve in Fig. 7 shows a typical x-y recorder data trace of the logarithm of the transmitted signal amplitude as a function of the magnetic field

strength. Most of the signal results from the large slowly varying monotonic background. The geometric resonances show up as minor perturbations on this background. The dominant frequency component of the geometric resonance signal is shown as the lower curve in Fig. 7, which is an x-y recorder trace of the "processed" data. The method of processing is described below.

The geometric resonances were periodic in H^{-1}. A special magnet sweep generator was constructed which made H^{-1} a linear function of time, i.e., $H^{-1} = \beta t$. Thus, the geometric resonances became periodic in time and normal electronic filtering techniques could be used to separate the resonances from the background and different resonant frequencies from each other. A block diagram of the apparatus used to do this is shown in Fig. 6. The details of these techniques are reported in Ref. 25.

The data obtained in this investigation were taken in magnetic fields of less than 300 G as a result of the large background attenuation. In these fields the resonances were almost always in the high-phase region ($\sim 30\pi$) so that errors resulting from low-phase deviations from Eq. (10) were negligible. All of the data were taken at 1.2°K to minimize the effects of electron-phonon scattering.

The experimentally determined resonant frequencies F were converted into extremal calipers using Eq. (10). The wavelength λ which enters this equation was determined using the velocity measurements of Eros

[25] J. B. Ketterson and Y. Eckstein, Rev. Sci. Instr. 37, 44 (1966).

and Smith,[26] together with the oscillator frequency. The velocities for longitudinal sound waves which were used are

$$V_{10\bar{1}0} = V_{11\bar{2}0} = 6.036 \times 10^5 \text{ cm/sec},$$

and   (12)

$$V_{0001} = 6.144 \times 10^5 \text{ cm/sec}.$$

The oscillator frequency was measured with a phase-cancellation technique accurate to 0.5%. All data were taken at 180 Mc/sec or 260 Mc/sec.

VI. EXPERIMENTAL RESULTS

Figure 8 shows a composite of most of the results obtained during the course of this investigation. For q parallel to $[10\bar{1}0]$ and $[11\bar{2}0]$, θ measures the angle between $[0001]$ and u in the $(10\bar{1}0)$ and $(11\bar{2}0)$ planes, respectively. u, as defined by Eq. (11), is the unit vector along which the external calipers are measured. For q parallel to $[0001]$, ϕ measures the angle between $[10\bar{1}0)]$ and u in the (0001) plane. The extremal calipers are plotted in atomic units. The calipers are accurate to about 2%; the angles are accurate to within 1°.

Nine distinct resonance branches were observed for q parallel to $[10\bar{1}0]$, six distinct branches for q parallel to $[11\bar{2}0]$ and four distinct branches for q parallel to
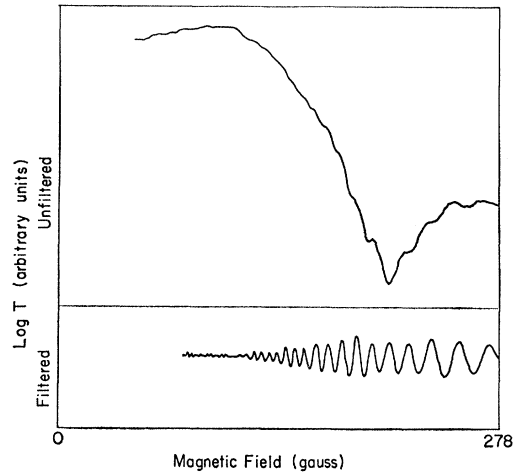

FIG. 7. Typical experimental data for q parallel to $[0001]$ and H in the basal plane. The upper trace shows the unprocessed data directly from the receiver (the receiver had logarithmic response). The lower trace shows the data after being electronically processed.

$[0001]$. In addition, several other frequency branches were detected at various points in these planes. These, however, did not have a large enough amplitude to be accurately resolved from the dominant branches. Each of the branches which are shown in Fig. 8 have been
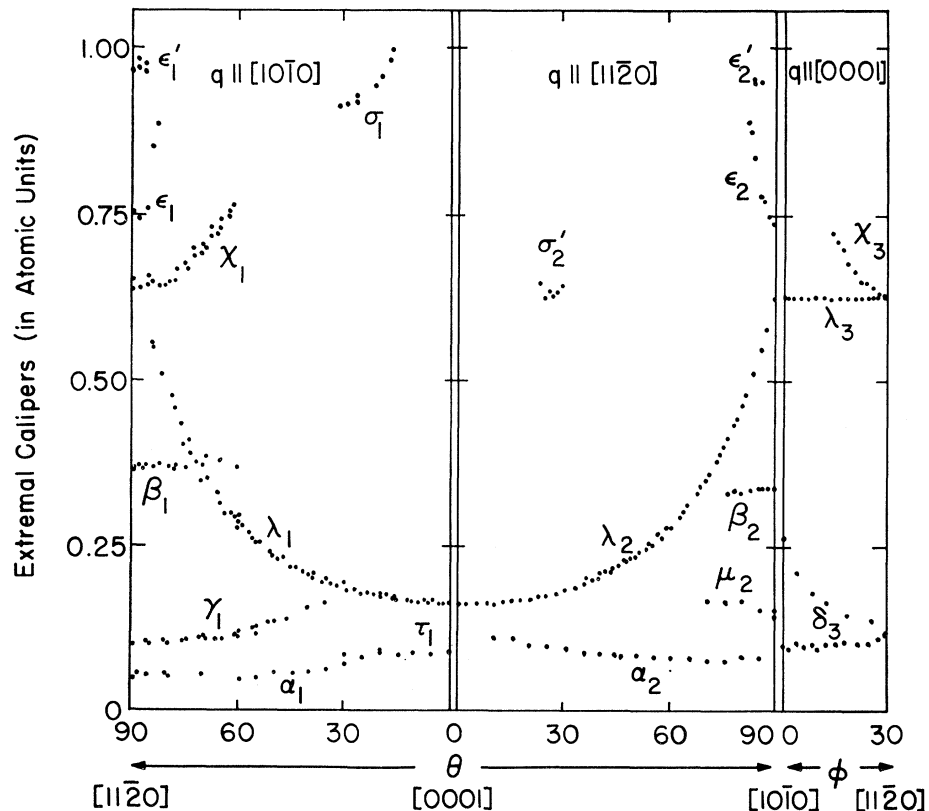

FIG. 8. The calipers measured (in a.u.) from the observed geometric resonances for q parallel to $[10\bar{1}0]$, $[11\bar{2}0]$, and $[0001]$. All data were taken at 180 or 260 Mc/sec.

[26] S. Eros and C. S. Smith, Acta Met. 9, 14 (1961).

designated by a Greek letter. The subscripts 1, 2, and 3 refer to calipers in the $(10\bar{1}0)$, $(11\bar{2}0)$, and (0001) planes, respectively.

The branches λ_1, λ_2, and λ_3 have been assigned to the lens. The resonances associated with these branches had the largest amplitude of any of the resonant branches of λ_1, and λ_2 was large enough to obscure other frequencies in that region. Thus we were unable to accurately resolve resonant branches associated with extremal calipers of about 0.5 a.u. (atomic units) for $\theta \lesssim 60°$.

β_1 and β_2 have been assigned to the butterflies. For $\theta = 90°$, β_1 (90) measures the extension of the butterfly along the LH zone line in the HAL plane. The butterfly cross section in this plane is that of a convex lens elongated along LH. Thus we expected and observed that for $\theta = 90°$, $\beta_2(90) = (\sqrt{3}/2)\beta_1(90)$. These branches could not be followed to small values of θ because of the large amplitude of the λ_1 and λ_2 branches and their harmonics.

γ_1 has been assigned to the cigar. Although it had a relatively large amplitude in the $(10\bar{1}0)$ plane it was not observed in the $(11\bar{2}0)$ plane. Some evidence was observed for this branch near $\varphi = 30°$ in the (0001) plane but its amplitude was too small to be accurately resolved. The γ_1 branch was ultimately obscured by the λ_1 branch.

The α_1, α_2, δ_3, ϵ_1, ϵ_2, ϵ_1', ϵ_2', χ_1, χ_3, σ_1, and σ_2' branches have all been assigned to various calipers on the monster. The α branches have been assigned to the diagonal arms of the monster. These are the arms shown in Fig. 3(a) which are directed toward the symmetry point H. The δ branch has been assigned to the monster waist [shown in Fig. 3(a) near the symmetry point M]. The ϵ, χ, and σ branches will be discussed in detail in the next section. The μ_2 branch does not seem to fit any of the extremal calipers that are predicted by our Fermi-surface model. However, as we shall discuss in the next section, it is quite possible that μ_2 may measure a nonextremal caliper.

VII. CALIPER ASSIGNMENTS

The lens is the only sheet of the magnesium Fermi surface which has symmetry sufficient to allow the unique conversion of all of its extremal calipers into radius dimensions. The λ_1, λ_2, and λ_3 extremal caliper branches have been assigned to the lens. The isotropic λ_3 caliper measures the extremal dimension of the lens about Γ in the ΓKM plane. The number n of resonant oscillations that occur in the range between a given field H_1 and $H = \infty$ is $n = F/H_1$, where F is defined by Eq. (10). $n \approx 30$ for the λ_3 frequency when $H_1 = 100$ G. The λ_3 oscillations remain phase locked to within 0.15 cycles for different directions of H in the (0001) plane when $H = 100$ G. Thus, $\Delta n < 0.15$ and

$$\frac{\Delta n}{n} = \frac{\Delta F}{F} = \frac{\Delta k_{\text{ext}}}{k_{\text{ext}}} = \frac{\Delta\lambda_3}{\lambda_3} < 0.005. \qquad (13)$$
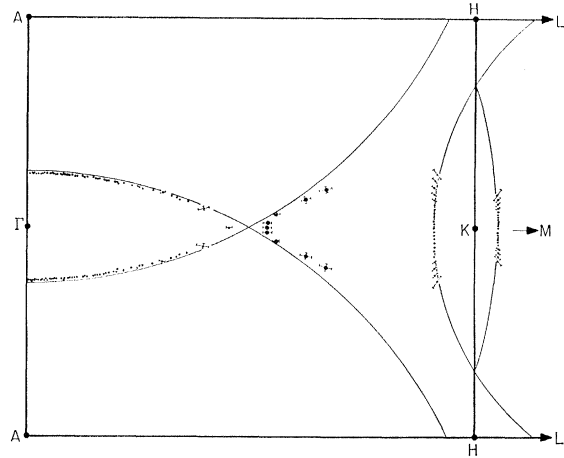

FIG. 9. The cross section in the ΓKHA plane of the lens, monster, and cigar sheets of the Fermi surface as constructed from the experimental data. The single-OPW contours are shown for comparison.

The radius of the lens about Γ in the ΓKM plane is then isotropic to within $\frac{1}{2}\%$.

The λ_1 and λ_2 branches measure the radius of the lens about Γ in the ΓKHA and the ΓMLA planes, respectively. The radii plotted in the ΓKHA plane are shown in Fig. 9. The cross sections of the single-OPW model are also shown for comparison. Notice how closely the experimental radii follow the single-OPW contour. The only major deviations occur as the surface crosses the ΓKM plane. This perturbation results, to first order, from the v_{0002} coefficient in the Fourier expansion of the pseudopotential [Eq. (8)]. The radii plotted in the ΓMLA plane are shown in Fig. 10. The cross sections
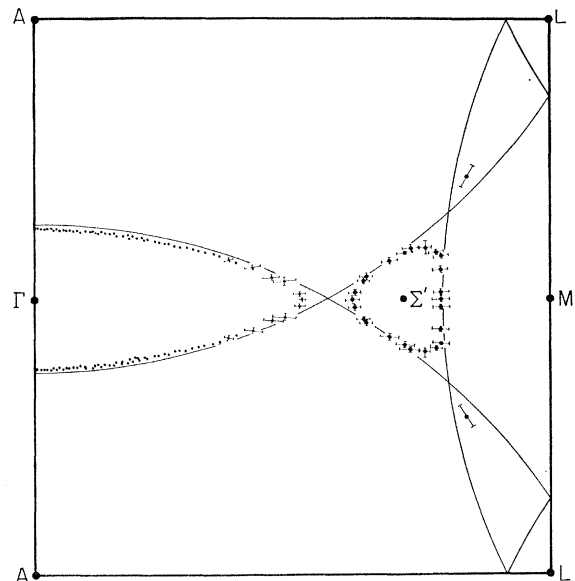

FIG. 10. The cross section in the ΓMLA plane showing both the experimentally constructed surfaces and the single-OPW contours.

FERMI SURFACE OF Mg. I

of the single-OPW model are again shown for comparison. Notice that the experimental radii in this plane are practically identical to the experimental radii in the ΓKHA plane. This together with the isotropy of the radii in the ΓKM plane suggests that the lens is very nearly a surface of revolution about the ΓA line.

The experimental radius along ΓA, $k_{\mathrm{LENS}}{}^{\Gamma A}$, is 0.058 a.u. and the experimental radii along both ΓK and ΓM, $k_{\mathrm{LENS}}{}^{\Gamma K, \Gamma M}$, are 0.313 a.u. These values are in sharp contradiction to the values of 0.094 and 0.217 a.u., respectively, deduced by Priestley[3] from his pulse-field de Haas–van Alphen measurements in magnesium. Reference 5 shows that this results from the misidentification of a de Haas–van Alphen frequency branch. The single-OPW value for $k_{\mathrm{LENS}}{}^{\Gamma K, \Gamma M}$ is 0.341 a.u. The difference Δ_{LENS} between the experimental value and the OPW value is $\Delta_{\mathrm{LENS}} = 0.028$ a.u.

When H is within $7°$ of the (0001) direction $(\theta \gtrsim 83°)$ extremal calipers are measured for orbits going about the inside and about the outside of the monster waist. Representative orbits of this group are shown sketched on the monster in Fig. 11. Sections of the monster showing these orbits in the ΓKH plane for H parallel to (0001) are shown in Figs. 4(a) and 4(b). These orbits are centered on Γ and are symmetric about the line of intersection of the orbit plane and the ΓKM plane. Thus their extremal calipers $(\epsilon_1, \epsilon_2, \epsilon_2')$ can be converted uniquely into radius dimensions.

Perhaps the most interesting set of radii are obtained from the ϵ_2 and ϵ_2' branches. These measure the dimensions $k_{\mathrm{IN}}{}^{\Gamma M}$ and $k_{\mathrm{OUT}}{}^{\Gamma M}$, respectively, as shown in Fig. 4(a). The ϵ_2 and ϵ_2' radii are plotted in the ΓMLA plane in Fig. 10. Note that these two branches nearly completely determine the cross section, centered on Σ', of the monster waist in this plane. The experimental cross section deviates from the single-OPW cross section primarily by rounding off the sharp corners of the OPW model. The rounding off as the surface cuts across the ΓKM plane results, in first order, from the v_{0002} coefficient of the potential. The rounding off of the two
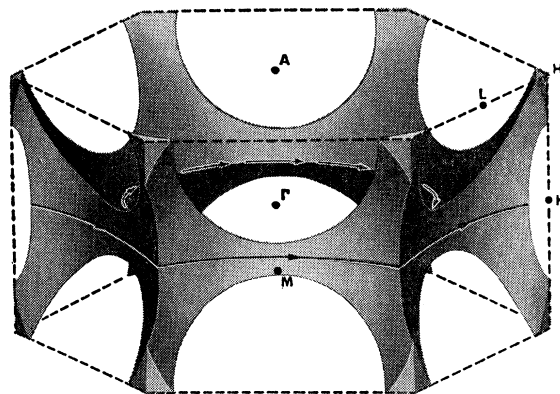

Fig. 11. Typical orbits around the inside and around the outside of the monster for H parallel to [0001]. The cross section in this orbit plane is shown in Figs. 4(a) and 4(b).

corners toward L result, in first order, from the $v_{10\bar{1}1}$ coefficient of the potential.

The ϵ_1 branch measures the radius $k_{\mathrm{IN}}{}^{\Gamma K}$ in the ΓKHA plane. These are shown in Fig. 9. We find experimentally that the $k_{\mathrm{IN}}{}^{\Gamma K}$ and $k_{\mathrm{IN}}{}^{\Gamma M}$ are equal in magnitude having a value of 0.370 a.u. This compares with the single-OPW value of 0.341 a.u. The difference Δ_{IN} between the experimental and single-OPW values is $\Delta_{\mathrm{IN}} = 0.029$ a.u.

Δ_{LENS} and Δ_{IN}, then, are essentially equal in magnitude. This, together with the fact that the calipers of both the lens and the inside of the monster waist are isotropic in the ΓKM plane, suggests that a first-order perturbation calculation using only two OPW's will yield a reasonable estimate of the value of the v_{0002} pseudopotential coefficient. We will obtain a value for this coefficient later in this paper.

The next caliper assignments which we will discuss will be those relevant to the butterflies. These assignments can not be made uniquely for most directions of H; they can, however, be made unambiguously using the single-OPW model as a guide. Figure 12(a) shows the cross section of the butterfly in the ΓALM plane

Fig. 12. Cross section in the ΓMLA plane of the butterfly–fourth-zone-electron-pocket complex. The two bands are degenerate in this plane along the LA line. (a) The butterfly orbit; (b) the coupled orbit; (c) the fourth-zone orbit.

$0.37 \pm .03$ a.u.

$0.23 \pm .02$ a.u.

0.087 ± 0.07 a.u.

(a)   (b)   (c)
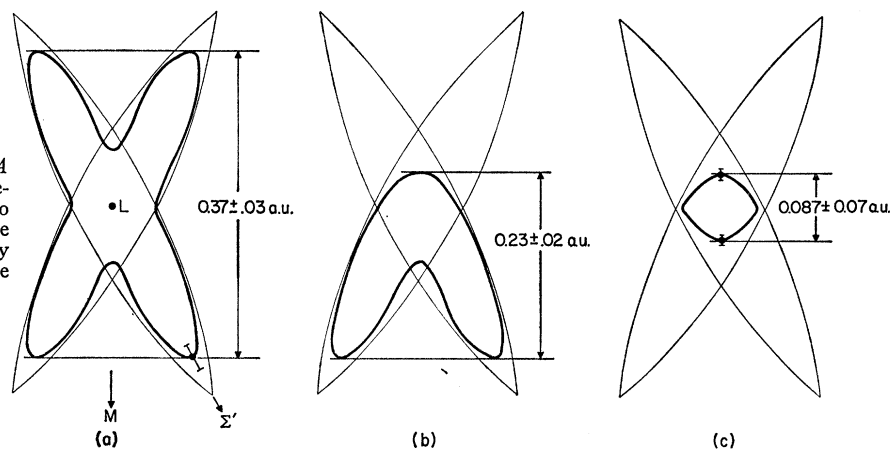
for **H** parallel to LH [$11\bar{2}0$], and **q** parallel LA [$10\bar{1}0$]; cross sections of both the single-OPW model and the "real" butterfly are shown. The experimental caliper (0.37 a.u.) measures the projection of this orbit on the LM line. The most useful information, of course, is not this projected length but the actual length of the butterfly tip from L to Σ'. Since the tip is centered on the ($10\bar{1}1$) plane of the third Brillouin zone and L lies in that plane, the orbit projections along the LM line can be transformed to a length measured on the ($10\bar{1}1$) plane with a high degree of accuracy. This transformation can be made for arbitrary directions of H as long as q is parallel to [$10\bar{1}0$].

Figure 13(a) shows the second Brillouin zone of magnesium. The butterflies occur as overlaps across the ($10\bar{1}1$)-type faces of the zone in the extended zone scheme. Fig. 13(b) shows a ($10\bar{1}1$) face with the transformed values of the β_1 extremal caliper branch plotted as butterfly radii about L. The intersection of the single-OPW spherical Fermi surface with this plane is also shown. The most notable feature of the data is that it shows that the real butterfly is not much smaller than the single-OPW model butterfly. The radius of the butterfly k_{BF}^{LH} from L along the LH line is 0.184 a.u. compared with a single-OPW value of 0.252 a.u. Falicov's band-structure calculations, on the other hand, seriously underestimate this dimension, giving a value of only 0.043 a.u.

The second interesting feature that shows up in the experimental data is an apparent anisotropy in the linear perturbation of the butterfly from the single-OPW model in this plane. This is probably due to the near proximity of other zone planes, in particular, the ($10\bar{1}0$) plane which intersects the ($10\bar{1}1$) plane along the LH line and the ($10\bar{1}1$) plane and (0002) plane which intersects the ($10\bar{1}1$) face along its edges parallel to the LH line.

The β_2 branch also measures the dimensions of the butterflies. In this case the orbits are projected onto a line in the ALH plane making an angle of 30° with the
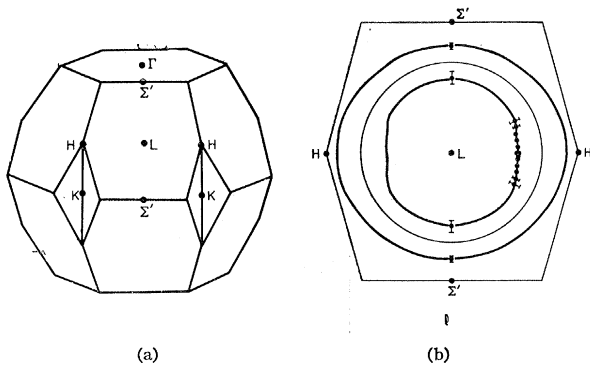
LH line. The β_2 calipers can not be uniquely or even unambiguously reduced into radius dimensions for the butterfly. For H parallel to [0001], β_2 (90)=0.335 a.u. compared with the projected value of β_1 on this line, $\sqrt{\frac{3}{2}}\,\beta_1$ (90)=0.318 a.u. The former is slightly greater than the latter as expected for a surface with a positive radius of curvature.

The γ_1 extremal caliper branch has been assigned to the cigar. This sheet of the Fermi surface is centered about K but does not have inversion symmetry about this point. Hence, the γ_1 branch can not be reduced to Fermi surface radii. The cigar does, however, have mirror symmetry across the ΓKHA plane. The γ_1 branch measures the calipers of the cigar in this plane about K. Reference 5 shows that the general shape of the cigar is very nearly that of the single-OPW model. We have thus plotted the γ_1 calipers in Fig. 9 using the single-OPW cross sections as a guide. This plot illustrates a significant point. The "real" cigar is a little larger than the single-OPW cigar along the ΓK line. In addition the calipers indicate that the "real" cigar is more cylindrical parallel to the KH line than in the single-OPW model. These conclusions are in accord with those reached in Ref. 5.

The α branches have been assigned to the diagonal arms of the monster. They are about a factor of 1.7 smaller than the dimensions of the diagonal arms on the single-OPW monster but their angular variation fits the variation expected. In addition, the de Haas–van Alphen measurements of Gordon et al.,[2] show that the cross-section area of the diagonal arms is about 3.4 times smaller than on the single-OPW model. This area reduction is thus just about right to go along with the dimension reduction discussed above.

The δ_3 branch has been assigned to the caliper of the monster waist in the ΓMK plane. Notice in Fig. 4(a) that the waist caliper parallel to ΓM, $C_{WAIST}^{\Gamma M}$, should be equal in magnitude to the quantity ($k_{OUT}^{\Gamma M} - k_{IN}^{\Gamma M}$). The experimental value of $C_{WAIST}^{\Gamma M}$ is 0.10 a.u. The experimental value of ($k_{OUT}^{\Gamma M} - k_{IN}^{\Gamma M}$) is 0.106 a.u. These agree within the experimental error and offer further confirmation of our assignments. The angular variation of the δ_3 branch agrees quite well with that expected from the single-OPW model if we include the added perturbation due to the v_{0002} coefficient of the pseudopotential discussed earlier.

The τ_1 branch has been assigned to the fourth-zone hole pocket centered on L. The caliper at $\theta = 0°$ ([0001]) measures the extension of the pocket along the LM line. This caliper can be converted directly into a radius dimension since this pocket has both reflection and inversion symmetry. The experimental radius of the pocket (P) from L along the LM line is $k_P^{LM} = 0.043$ a.u. The cross section of the pocket in the ΓMLA plane is shown in Fig. 12(c).

Two other calipers which have been assigned to the butterfly-fourth-zone-pocket complex were observed for

(a)　　　　　　　　(b)

FIG. 13. (a) The second Brillouin zone of magnesium showing the pertinent symmetry points. The point Σ' designates the intersection of the Σ (ΓM) zone line with the ($10\bar{1}1$) zone face. (b) The intersection of the ($10\bar{1}1$) zone face with the monster and the butterfly in the extended zone scheme.

this same orientation of **H** and **q**. One measures the extension of the butterfly along the *LM* line as discussed earlier. The experimental value obtained for this caliper is $C_{BF}{}^{LM}=0.37$ a.u. The corresponding cross section is shown in Fig. 10(a). The second caliper has a value of $C_{COUPLED}{}^{LM}=0.23$ a.u. This has been assigned to the coupled orbit shown in Fig. 12(a). The spin-orbit-coupling induced energy gap which separates the butterfly and the fourth-zone-pocket in the *ALH* plane vanishes along the *AL* line. Thus the electron orbits in the ΓMHA plane should be those shown in Fig. 12(b). The gap increases as k^3 out of this plane[18] so the orbits out of this plane are those for the butterfly [Fig. 12(a)] and the fourth-zone-pocket [Fig. 12(c)]. Magnetic breakdown effects will of course create a region of finite thickness about the ΓMLA plane in which all three of these orbits exist simultaneously. For consistency, $C_{COUPLED}{}^{LM}$ should be equal in magnitude to
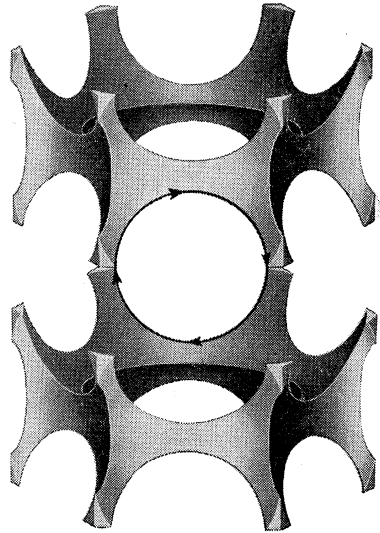

FIG. 14. A $(10\bar{1}1)$ plane orbit on the monster in the repeated zone scheme for **u** in the direction defined by $\theta\simeq28.5°$; $\varphi=0°$.

$\frac{1}{2}C_{BF}{}^{LM}+k_P{}^{LM}=0.228$ a.u. This agrees quite well with the experimental value of $C_{COUPLED}{}^{LM}$.

The σ_2' branch has been assigned to an orbit on the monster in the *repeated* zone scheme. One of these orbits is shown in Fig. 14 for **H** parallel to the $[10\bar{1}1]$ direction $(\theta\simeq28.5°)$. Note that for this field direction the orbit plane coincides with the $(10\bar{1}1)$ zone plane shown in Fig. 13. The intersection of the monster in the *extended* zone scheme with the $(10\bar{1}1)$ plane shown in Fig. 13(b) defines this orbit. For this orientation of **H**, the σ_2' branch yields the radius of the monster in the extended zone scheme along the $A\Sigma'$ line. The experimental value of this radius is $k_{MONSTER}{}^{A\Sigma'}=0.65$ a.u. When **H** is tilted from $[10\bar{1}1]$, the σ_2' branch yields the radius from A of the monster waist in the ΓMLA plane.

The σ_1 branch has also been assigned to an orbit on the monster in the *repeated* zone scheme. The cross section of this orbit is shown in Fig. 15. The caliper of the orbit shown is extremal for the single-OPW model.
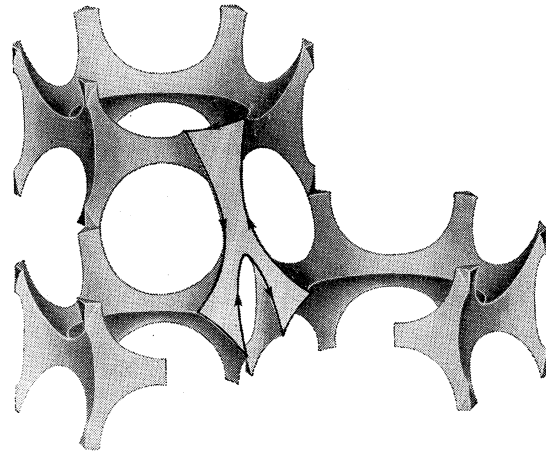

FIG. 15. A repeated zone orbit on the monster for **u** in the direction $\theta\simeq20°$; $\varphi=30°$.

At $\theta=20°$, the experimental caliper of 0.952 a.u. compares quite well with the value of 1.005 a.u. predicted by the single-OPW model. The most significant point that can be made about these multizone calipers is that they were observed to have relatively large amplitudes in magnetic fields as large as 300 G. This means that the spin-orbit-coupling-induced energy gap across the *ALH* plane is sufficiently large in the immediate neighborhood of H that magnetic breakdown across this gap is not too significant in magnetic fields as large as 300 G. This is the first reported direct experimental evidence for the existence of this gap near H.

The χ_1 branch has been assigned to the nonextremal caliper C_{TIP} of the hexagonal-shaped orbit around the outside of the monster waist. This orbit as well as C_{TIP} is shown in Fig. 4(b) for $\theta=90°$. The reasons that this nonextremal dimension contributes a geometric resonance have been discussed in Sec. IV. The experimental value obtained for C_{TIP} is 0.622 a.u. We note in Fig. 4(b) that C_{TIP} forms one side of the equilateral triangle $TT'T$. Thus, the radius dimension $k_{OUT}{}^{\Gamma K}$ must be identically equal to C_{TIP}.

We did not observe the geometric resonance associated with the caliper $2k_{OUT}{}^{\Gamma K}$. However, we have assigned the caliper ϵ_1' to the dimension $(k_{OUT}{}^{\Gamma K}+\frac{1}{2}C_{TIP})=1.5 \ C_{TIP}=0.95$ a.u. This is shown in Fig. 4(b). The experimental value of ϵ_1' is 0.97 a.u. This agrees with the predicted value within the error of ϵ_1'.

The branch χ_3 also measures the caliper C_{TIP} when $\phi=30°$. In this case, however, the caliper is measured on quite a different shaped orbit than that shown in Fig. 4(b). Figure 16 shows the location and shape of this orbit on the monster. Here the dimension C_{TIP} is extremal in a given orbit plane but is not extremal for a succession of orbit planes cut parallel to H. The cutoff which gave rise to the χ_1 geometric resonance was a cutoff in the electron-phonon energy exchange integral. In this case the cutoff which gives rise to the χ_3 geo-
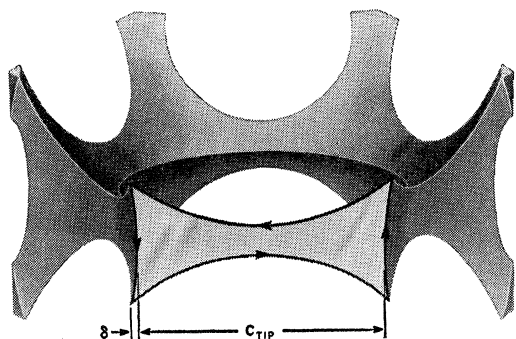
Fig. 16. The orbit responsible for the geometric resonance signal showing the giant amplitude growth shown in the lower trace in Fig. 17 at $H\simeq125$ G. H was parallel to [10$\bar{1}$0] with q parallel to [0001].

metric resonance is a cutoff in the phase integral for successive orbit planes.

An interesting "giant" growth in the amplitude of the X_3 geometric resonance oscillations was observed for $H\simeq125$ G. The upper curve in Fig. 17 shows a trace of the geometric resonance oscillations arising from the λ_3 branch (lens) for $\varphi=0°$. Here, there is only the one pure λ_3 frequency. Its amplitude growth as a function of H is essentially that predicted by theory. For a given value of H the amplitude of the λ_3 branch was found to be independent of φ. At $\varphi=30°$, X_3 is almost degenerate with λ_3. The lower curve in Fig. 17 shows a trace of the sum of the geometric resonance oscillations from the X_3 and λ_3 branches for $\phi=30°$. Below 125 G the X_3 oscillations are nearly in phase with the λ_3 oscillations and the X_3 amplitude is about $\frac{1}{2}$ the λ_3 amplitude. At about 125 G the amplitude of the X_3 oscillations begins to increase very rapidly and by 175 G the X_3 amplitude is about four times as large as the λ_3 amplitude.

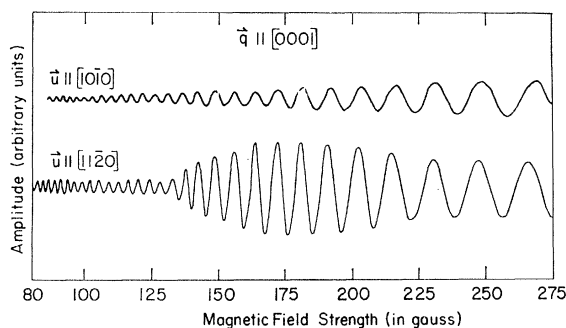We attribute this giant amplitude growth to the peculiar shape of the orbit shown in Fig. 16. Notice

Fig. 17. The upper curve shows the geometric resonance oscillations arising from the lens for H parallel to [11$\bar{2}$0]. The lower shows the sum of the geometric resonance oscillations arising from the lens and the monster orbit shown in Fig. 16. For $H\lesssim125$ G the lens amplitude is dominant in the lower curve. For $H\gtrsim125$ G the orbit shown in Fig. 16 is dominant.

that this orbit has six turning points. Three of these on each end are separated by the small distance δ. When δ becomes less than $\lambda/2$, the ends of this orbit look essentially flat with respect to the sound waves. Thus the electron-phonon energy-exchange integrals yield a much greater net exchange and the amplitude of the X_3 oscillations shows a considerable increase. This condition is expected to occur at about 100 G on the single-OPW model.

The μ_2 branch has been assigned to a nonextremal caliper on the butterfly. The geometry of the orbits which are associated with this caliper was discussed earlier in the Sec. IV. The geometric resonances arise as a result of a saddle-point cutoff in the phase integral along H. The experimental value of μ_2 at $\theta=90°$ is 0.15 a.u. compared with the single-OPW value of 0.18 a.u. The former is a little smaller than the latter but the disagreement is in the expected direction. A finite value for the $v_{10\bar{1}1}$ pseudopotential coefficient will reduce the amount of overlap across the (10$\bar{1}$1) face of the Brillouin zone and hence reduce the dimension of the butterfly at the saddle-point cutoff.

A tabulation of all of the important experimentally determined Fermi-surface dimensions along symmetry lines of the Brillouin zone is shown in Table II. Also included for comparison are the single-OPW dimensions as well as those resulting from Falicov's band-structure calculations. Note that in general the experimental dimensions are in closer agreement with the single-OPW model than with Falicov's model.

VIII. ESTIMATES OF THE PSEUDO-POTENTIAL COEFFICIENTS

Perhaps the most significant result of this investigation is that the actual Fermi surface of magnesium shows only very small departures from the single-OPW model. This is true for all of the sheets of the Fermi surface. We can thus proceed with confidence to estimate the coefficients of the Fourier expansion of the pseudopotential [Eq. (8)] using first-order degenerate perturbation theory[27] in the vicinity of a Bragg reflection plane associated with a given reciprocal lattice vector G_i. These coefficients can be expected to be quite accurate providing that they are calculated in regions of the extended zone scheme where the Fermi surface intersects and is close to only a single Bragg plane. In this case the pseudo-wave function φ can be represented as a linear combination of two plane waves, i.e.,

$$\varphi=A_0e^{i\mathbf{k}\cdot\mathbf{r}}+A_ie^{i(\mathbf{k}-\mathbf{G}_i)\cdot\mathbf{r}}. \qquad (14)$$

When this wave function is substituted into the modi-

[27] N. F. Mott and H. Jones, *The Theory of the Properties of Metals and Alloys* (Dover Publications, Inc., New York, 1958), p. 59.

TABLE II. Fermi-surface dimensions (in atomic units).

Experimental	SOPW	Falicov
2nd-zone monster		
Inside		
$k_{IN}^{\Gamma K, \Gamma M} = 0.370$	$k_{IN}^{\Gamma K, \Gamma M} = 0.341$	$k_{IN}^{\Gamma K} = 0.405$
$\Delta_{IN} = k_{IN}^{\Gamma K, \Gamma M}(SOPW) - k_{IN}^{\Gamma K, \Gamma M}(exp) = 0.029$		$k_{IN}^{\Gamma M} = 0.415$
Outside		
$k_{OUT}^{\Gamma M} = 0.476$	$k_{OUT}^{\Gamma M} = 0.476$	$k_{OUT}^{\Gamma M} = 0.452$
$k_{OUT}^{\Gamma K} = 0.622$	$k_{OUT}^{\Gamma K} = 0.634$	$k_{OUT}^{\Gamma K} = 0.606$
Waist		
$C_{WAIST}^{\Gamma M} = 0.100$	$C_{WAIST}^{\Gamma M} = 0.135$	$C_{WAIST}^{\Gamma M} = 0.037$
$k_{OUT}^{\Gamma M}(exp) - k_{IN}^{\Gamma M}(exp) = 0.106$		
$k_{WAIST}^{\Sigma' L} = 0.064$	$k_{WAIST}^{\Sigma' L} = 0.110$	$k_{WAIST}^{\Sigma' L} = 0.062$
3rd-zone lens		
$k_{LENS}^{\Gamma A} = 0.080$	$k_{LENS}^{\Sigma A} = 0.085$	$k_{LENS}^{\Gamma A} = 0.058$
$k_{LENS}^{\Gamma K, \Gamma M} = 0.312$	$k_{LENS}^{\Gamma K, \Gamma M} = 0.341$	$k_{LENS}^{\Gamma K} = 0.253$
$\Delta_{LENS} = k_{LENS}^{\Gamma K, \Gamma M}(SOPW) - k_{LENS}^{\Gamma K, \Gamma M}(exp) = 0.029$		$k_{LENS}^{\Gamma M} = 0.255$
3rd-zone cigar		
$C_{CIGAR}^{\Gamma K M} = 0.100$	$C_{CIGAR}^{\Gamma K M} = 0.093$	$C_{CIGAR}^{\Gamma K M} = 0.117$
$k_{CIGAR}^{K\Gamma} \simeq 0.067$	$k_{CIGAR}^{K\Gamma} = 0.062$	$k_{CIGAR}^{K\Gamma} = 0.073$
$k_{CIGAR}^{K M} \simeq 0.033$	$k_{CIGAR}^{K M} = 0.031$	$k_{CIGAR}^{K M} = 0.044$
3rd-zone butterfly		
$k_{BF}^{L H} = 0.184$	$k_{BF}^{L H} = 0.252$	$k_{BF}^{L H} = 0.043$
$k_{BF}^{L \Sigma'} = 0.206$	$k_{BF}^{L \Sigma'} = 0.252$	
4th-zone pocket		
$k_P^{L M} = 0.043$	$k_P^{L M} = 0.090$	$k_P^{L M} = 0.029$

fied wave equation (7) the secular equation

$$\begin{vmatrix} k^2 - E & S(\mathbf{G}_i)v_{\mathbf{G}_i} \\ S^*(\mathbf{G}_i)v_{\mathbf{G}_i}^* & (\mathbf{k} - \mathbf{G})^2 - E \end{vmatrix} = 0 \qquad (15)$$

results. The solutions of this equation are

$$E^{\pm} = \tfrac{1}{2}[k^2 + (\mathbf{k} - \mathbf{G}_i)^2] \pm \{\tfrac{1}{4}[k^2 + (\mathbf{k} - \mathbf{G}_i)^2]^2 \\ - k^2(\mathbf{k} - \mathbf{G}_i)^2 + |S(\mathbf{G}_i)|^2 |v_{\mathbf{G}_i}|^2\}^{1/2}. \qquad (16)$$

We will evaluate this using experimentally determined dimensions on a given Bragg plane. In this case the Bragg reflection condition $|\mathbf{k}|^2 = |\mathbf{k} - \mathbf{G}_i|^2$ reduces Eq. (16) to

$$E^+ = k_+^2 + |S(\mathbf{G}_i)| \, |v_{\mathbf{G}_i}| \,,$$
$$E^- = k_-^2 - |S(\mathbf{G}_i)| \, |v_{\mathbf{G}_i}| \,, \qquad (17)$$

where E^+ and E^- refer to the energies in two successive zones, E^+ referring to the zone of higher index. Since all of our experimental calipers determine $\mathbf{k}$ at the Fermi surface, we will only be interested in the case for which $E^+ = E^- = E_F = k_F^2$.

Figure 18 shows the constant energy surface E_F which results from the solution of Eq. (16) in the vicinity of the Bragg plane. Since $\mathbf{G}_i$ is normal to the plane in which the dimensions $k_+(exp)$ and $k_-(exp)$ are assumed to be determined, the solution of Eq. (17)

for $|v_{\mathbf{G}_i}|$ is simply

$$|v_{\mathbf{G}_i}| = \frac{k_-^2(exp) - k_+^2(exp)}{2|S(\mathbf{G}_i)|} = \frac{k_-^2(exp) - k_{SOPW}^2}{|S(\mathbf{G}_i)|}$$
$$= \frac{k_{SOPW}^2 - k_+^2(exp)}{|S(\mathbf{G}_i)|}, \qquad (18)$$

providing $|S(\mathbf{G}_i)| \neq 0$.

The magnesium Fermi surface intersects only three types of Brillouin zone planes for which $|S(\mathbf{G}_i)| \neq 0$. These are, in order of increasing $|\mathbf{G}_i|$, the $(10\bar{1}0)$, (0002) and $(10\bar{1}1)$ zone faces. The values of $S(\mathbf{G}_i)$ and $|\mathbf{G}_i|$ for each of these planes are tabulated in Table III.
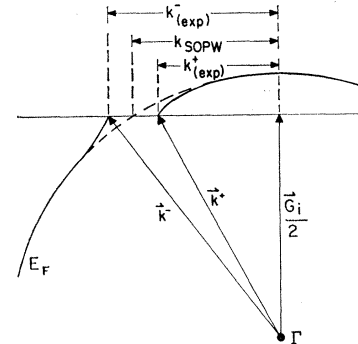
FIG. 18. Typical two-OPW perturbation contours.

Table III. Local pseudopotential coefficients obtained with the use of a two-orthogonalized-plane-wave approximation.

i	$|\mathbf{G}_i|$ (in atomic units)	$S(\mathbf{G}_i)$	$|v_{\mathbf{G}_i}|$ (in Ry)
[0001]	$2\pi/t_1 = 0.6424$	0	indeterminate
[10$\bar{1}$0]	$4\pi/\sqrt{3}t_2 = 1.2041$	$(1\pm i\sqrt{3})/2$	$\sim 5\times10^{-4}$
[0002]	$4\pi/t_1 = 1.2848$	2	0.010
[10$\bar{1}$1]	$2\pi[(1/t_1{}^2)+(4/3t_2{}^2)]^{1/2}$		
	$= 1.3647$	$(3\pm i\sqrt{3})/2$	0.017

$|v_{10\bar{1}0}|$: For this coefficient the pertinent experimental calipers are $k_{\text{OUT}}{}^{\Gamma K}$ and our deduced dimension $k_{\text{CIGAR}}{}^{K\Gamma}$ given in Table II. We note that their sum (0.688 a.u.) although slightly smaller is, within experimental error, equal to the ΓK dimension of the Brillouin zone ($3^{-1/2}G_{10\bar{1}0} = 0.695$ a.u.). Thus, $|v_{10\bar{1}0}|$ must be very small. The value of this pseudopotential coefficient was estimated in Ref. 9 from magnetic breakdown measurements to be approximately 5×10^{-4} Ry. This is so small that we can ignore its effects when computing the remaining pseudopotential coefficients.

$|v_{0002}|$: This coefficient can be determined using in Eq. (18) the dimension $k_{\text{LENS}}{}^{\Gamma K, \Gamma M}$ and $k_{\text{IN}}{}^{\Gamma K, \Gamma M}$ given in Table II. The value obtained for this pseudopotential coefficient is $|v_{0002}| = 0.010$ Ry.

$|v_{10\bar{1}1}|$: This pseudopotential parameter can be estimated using the dimensions $k_{\text{BF}}{}^{LH}$ and $k_{\text{BF,SOPW}}{}^{LH}$ given in Table II. The (10$\bar{1}$0) zone plane intersects the (10$\bar{1}$1) plane along the LH line but as we have shown $v_{10\bar{1}0}$ is negligibly small. Thus we can ignore its effects and estimate $v_{10\bar{1}1}$ using only two plane waves along this line. The value which we obtain for this coefficient is $v_{10\bar{1}1} = 0.017$ Ry. The two-OPW theory predicts that the intersection of the butterfly with the (10$\bar{1}$1) plane should be circular. This was not observed experimentally (see Fig. 13). This may be due to the distortion of the free-electron energy curves by the proximity of several other zone planes near Σ'.

The pseudopotential coefficients have been collected for reference in Table III.

IX. TWO-OPW ENERGY SURFACE FOR THE LENS

In this section we will use the experimentally deduced value of the v_{0002} pseudopotential coefficient in Eq. (16) in order to parametrize the lens Fermi surface. To do this it is convenient to transfer the origin of coordinates in k space, and also the zero of energy, to the point in the center of the lens. Equation (16) then yields

$$E' = k_x{}^2 + k_y{}^2 + k_z{}^2 + [k_z{}^2 G_{0002}{}^2 + 4v_{0002}{}^2]^{1/2} - 2|v_{0002}|, \quad (19)$$

where

$$E' = E_F - \tfrac{1}{4}G_{0002}{}^2 - 2|v_{0002}|, \quad (20)$$

and k_x is measured in a ΓM direction, k_y in a ΓK direction, and k_z in the ΓA direction.

Figure 19 shows the cross section of the lens Fermi surface in the ΓKA plane. The solid curve shows the

two-OPW controur obtained from Eq. (19). Both the single-OPW contour (light curve) and the experimentally determined radii are shown for comparison. It can be seen that the two-OPW approximation yields a good representation for the actual lens Fermi surface. We will use Eq. (19) to calculate further properties for the lens and compare these with existing experimental data.

When Eq. (19) is used to evaluate $k_{\text{LENS}}{}^{\Gamma A}$, we obtain a value of 0.084 a.u. compared with an experimental value of 0.080 a.u. and a single-OPW value of 0.085 a.u. This represents the maximum deviation of the two-OPW contour from the actual Fermi surface.

The cross-sectional area of the two-OPW surface in the $\Gamma M A$ plane was evaluated numerically. The resultant area of 0.0753 a.u. is to be compared with the de Haas–van Alphen area[5] of 0.0727, and the single-OPW area of 0.0786. A graphical integration of the area under the curve traced out by the geometric resonance radii yields 0.0715. The area in $\Gamma M K$ plane is $\pi(k_{\text{LENS}}{}^{\Gamma K, \Gamma M})^2 = 0.306$ a.u. compared with the de Haas–van Alphen area[5] of 0.308 a.u. and the single-OPW area of 0.365 a.u.

The effective mass in a.u. is given by

$$m^* = -\frac{1}{\pi}\frac{d\mathcal{Q}}{dE}, \quad (21)$$

where $\mathcal{Q}$ is the area enclosed by the pertinent orbit in k space. When $\mathbf{H}$ is along ΓA, both the single-OPW and two-OPW models give the identical result that $m_{\Gamma A}{}^* \equiv 1$. The experimental value of this mass obtained by cyclotron-resonance experiments[7] is $m_{\Gamma A}{}^* = 1.38$. The effective mass for $\mathbf{H}$ in the basal plane was obtained numerically for the two-OPW model using Eq. (21). This yielded a value of $m_{\text{BASAL}}{}^* = 0.315$ compared with the experimental value[6] of $m_{\text{BASAL}}{}^* = 0.42$ and a single-OPW value of 0.311. Because of many-body effects (electron-electron[28] and electron-phonon[29]) one does not expect the band-structure mass to agree with the experimental mass. They should in fact be related by

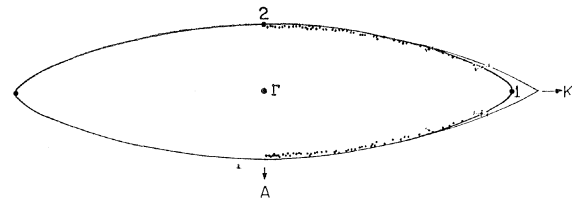$$m^*(\exp) = m^*(\text{band structure})(1 + \delta_{m^*e\text{-}e} + \delta_{m^*e\text{-}p}). \quad (22)$$

Fig. 19. The cross section in the ΓKA plane of the two-OPW-model lens. The experimental radii and the single-OPW contour are shown for comparison.

[28] T. M. Rice, Ann. Phys. (N. Y.) 31, 100 (1965).
[29] N. W. Ashcroft and J. W. Wilkins, Phys. Letters 14, 285 (1965).

Thus, if many-body effects are isotropic over the Fermi surface, the ratio of the two band-structure masses will be equal to the ratio of the two experimental masses. The band-structure mass ratio $(m_{\Gamma A}*/m_{\text{BASAL}}*)$ is 3.17 compared with the equivalent experimental mass ratio of 3.29. The fact that the former is slightly smaller than the latter seems to indicate that the many-body enhancement effects are slightly anisotropic, being smaller around the top of the lens than around the rim. Since our model is only approximate this difference should be viewed with caution. However, Zych's limiting-point cyclotron-resonance experiments have yielded a value for the limiting-point cyclotron mass in the ΓA direction of $m_{\Gamma A}*$ $(LP)=1.31$. We will show below that $m_{\Gamma A}*$ (LP) should be identically equal to the previously listed value of $m_{\Gamma A}*=1.38$ if the many-body enhancement effects are isotropic over the two-OPW surface. The fact that $m_{\Gamma A}*$ (LP) is smaller than $m_{\Gamma A}*$ agrees with the anisotropy shown by the mass ratios discussed above.

Reference 28 shows that $\delta_{m}*_{e\text{-}e}$ is about 0.01 for magnesium. Thus if we assume that all remaining difference is due to electron-phonon interactions $\delta_{m}*_{e\text{-}p}$ must be about 0.37 for orbits around the rim of the lens and about 0.30 for the limiting-point mass along ΓA.

In the remainder of this section we will be concerned with some of the aspects of our model which can be described in terms of geometrical radii of curvature. Each point i on the surface can be defined by two principle radii of curvature, $\rho_a{}^{(i)}$, and $\rho_b{}^{(i)}$,, measured in the mutually orthogonal a and b planes. The Gaussian radius of curvature $\rho_G{}^{(i)}$, at the point i is given by

$$\rho_G{}^{(i)} = [\rho_a{}^{(i)}\rho_b{}^{(i)}]^{1/2}. \qquad (23)$$

In the following discussion we will need the radii of curvature at the points labeled 1 and 2 in Fig. 19. The principle radii of curvature at these points are $\rho_{\Gamma MK}{}^{(1)}$; $\rho_{\Gamma MA}{}^{(1)}$ and $\rho_{\Gamma AM}{}^{(2)}$; $\rho_{\Gamma AK}{}^{(2)}$, respectively. These, as well as the electron velocity have been calculated for the two-OPW model and are listed in Table IV.

The value of the limiting-point cyclotron mass is given by the expression

$$m_i*(LP)v_i = (1/\pi)(d\mathcal{Q}_i/dk_H), \qquad (24)$$

where $\mathcal{Q}_i$ is the area enclosed by an electron orbit very near the limiting point i and v_i is the limiting point velocity. If $\mathcal{Q}_i$ is expressed in terms of the radii of curvature at i this reduces to

$$m_i*(LP) = 2\rho_G{}^{(i)}/v_i. \qquad (25)$$

Since the lens is a surface of revolution about ΓA, it is apparent that $\rho_G{}^{(2)} = \rho_{\Gamma AM}{}^{(2)} = \rho_{\Gamma AK}{}^{(2)}$. The values of $\rho_G{}^{(2)}$ and v_2 tabulated in Table IV show that m_2* (LP) $= m_{\Gamma A}* = 1$.

The geometric resonance amplitude factors discussed in Sec. IV reduce to an especially simple form for orbits on the lens. When $\mathbf{H}$ is parallel to $[0001]$ and $\mathbf{q}$ is parallel to either $[10\bar{1}0]$ or $[11\bar{2}0]$ the amplitude A_1

TABLE IV. Two-OPW lens parameters (in atomic units).

$$m_{\Gamma A}* = 1 \qquad\qquad m_{\text{BASAL}}* = 0.315$$

$$v_1 = 2k_{\text{LENS}}{}^{\Gamma K, \Gamma M} = 0.625$$

$$v_2 = 2k_{\text{LENS}}{}^{\Gamma A} + \frac{k_{\text{LENS}}{}^{\Gamma A}G_{0002}{}^2}{[(k_{\text{LENS}}{}^{\Gamma A})^2(G_{0002})^2 + 4v_{0002}{}^2]^{1/2}} = 1.424$$

$$\rho_{\Gamma MK}{}^{(1)} = k_{\text{LENS}}{}^{\Gamma k, \Gamma M} = 0.312$$

$$\rho_{\Gamma MA}{}^{(1)} = \frac{4v_{0002}k_{\text{LENS}}{}^{\Gamma K, \Gamma M}}{4v_{0002} + G_{0002}{}^2} = 0.0072$$

$$\rho_G{}^{(1)} = \rho_{\Gamma AM}{}^{(2)} = \rho_{\Gamma AK}{}^{(2)} = k_{\text{LENS}}{}^{\Gamma A}$$

$$+ \frac{\tfrac{1}{2}k_{\text{LENS}}{}^{\Gamma A}G_{0002}{}^2}{[(k_{\text{LENS}}{}^{\Gamma A})^2(G_{0002})^2 + 4v_{0002}{}^2]^{1/2}} = 0.712$$

of the geometric resonance measuring $k_{\text{LENS}}{}^{\Gamma K, \Gamma M}$ is

$$A_1 \propto \rho_{\Gamma MK}{}^{(1)}(\rho_{\Gamma MA}{}^{(1)})^{1/2}/(m_{\Gamma A}*v_1)^2. \qquad (26)$$

When $\mathbf{H}$ is parallel to either $[10\bar{1}0]$ or $[11\bar{2}0]$ and $\mathbf{q}$ is parallel $[0001]$ direction, the amplitude A_2 of the geometric resonance measuring $k_{\text{LENS}}{}^{\Gamma K, \Gamma M}$ is

$$A_2 \propto \rho_{\Gamma MA}{}^{(1)}(\rho_{\Gamma MK}{}^{(1)})^{1/2}/(m_{\text{BASAL}}*v_1)^2. \qquad (27)$$

When $\mathbf{H}$ is parallel to either $[10\bar{1}0]$ or $[11\bar{2}0]$ and $\mathbf{q}$ is parallel to either the appropriate $[11\bar{2}0]$ or $[10\bar{1}0]$ direction, respectively, the amplitude A_3 of the geometric resonance measuring $k_{\text{LENS}}{}^{\Gamma A}$ is

$$A_3 \propto (\rho_{\Gamma AM}{}^{(2)})^{3/2}/(m_{\text{BASAL}}*v_2)^2. \qquad (28)$$

These have been evaluated using the values tabulated in Table IV. Their predicted ratios $A_1:A_2:A_3 = 1:1.8:52$ are in qualitative agreement with the observed experimental amplitude ratios.

X. CONCLUSIONS

The magnetoacoustic measurements reported in this paper have shown that the Fermi surface of magnesium is much more free-electron-like than previously believed. The data pertinent to the lens and butterflies in the third Brillouin zone show that these pieces are only slightly smaller than in the single-OPW model. We were thus encouraged to estimate the various local pseudopotential coefficients using a two-OPW approximation. The values obtained for these coefficients (listed in Table III) are probably accurate to within 0.002 Ry.

The observation of geometric resonances associated with multizone calipers on the monster show that magnetic breakdown of the spin-orbit-coupling-induced energy gap near point H in the AHL zone plane is not too significant in magnetic fields as high as 300 G.
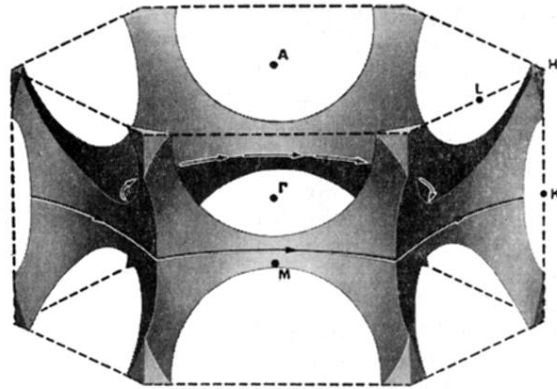
ACKNOWLEDGMENTS

Fig. 11. Typical orbits around the inside and around the outside of the monster for **H** parallel to [0001]. The cross section in this orbit plane is shown in Figs. 4(a) and 4(b).

FIG. 14. A (10$\bar{1}$1) plane orbit on the monster in the repeated zone scheme for **u** in the direction defined by $\theta \simeq 28.5°$; $\varphi = 0°$.
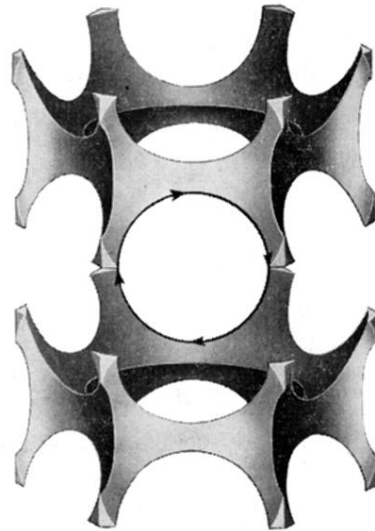
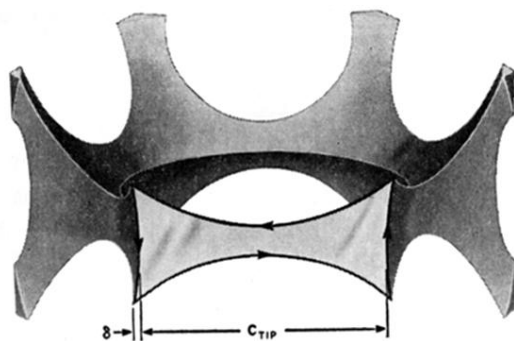FIG. 15. A repeated zone orbit on the monster for **u** in the direction $\theta \simeq 20°$; $\varphi = 30°$.

FIG. 16. The orbit responsible for the geometric resonance signal showing the giant amplitude growth shown in the lower trace in Fig. 17 at $H \simeq 125$ G. $\mathbf{H}$ was parallel to $[10\bar{1}0]$ with $\mathbf{q}$ parallel to $[0001]$.
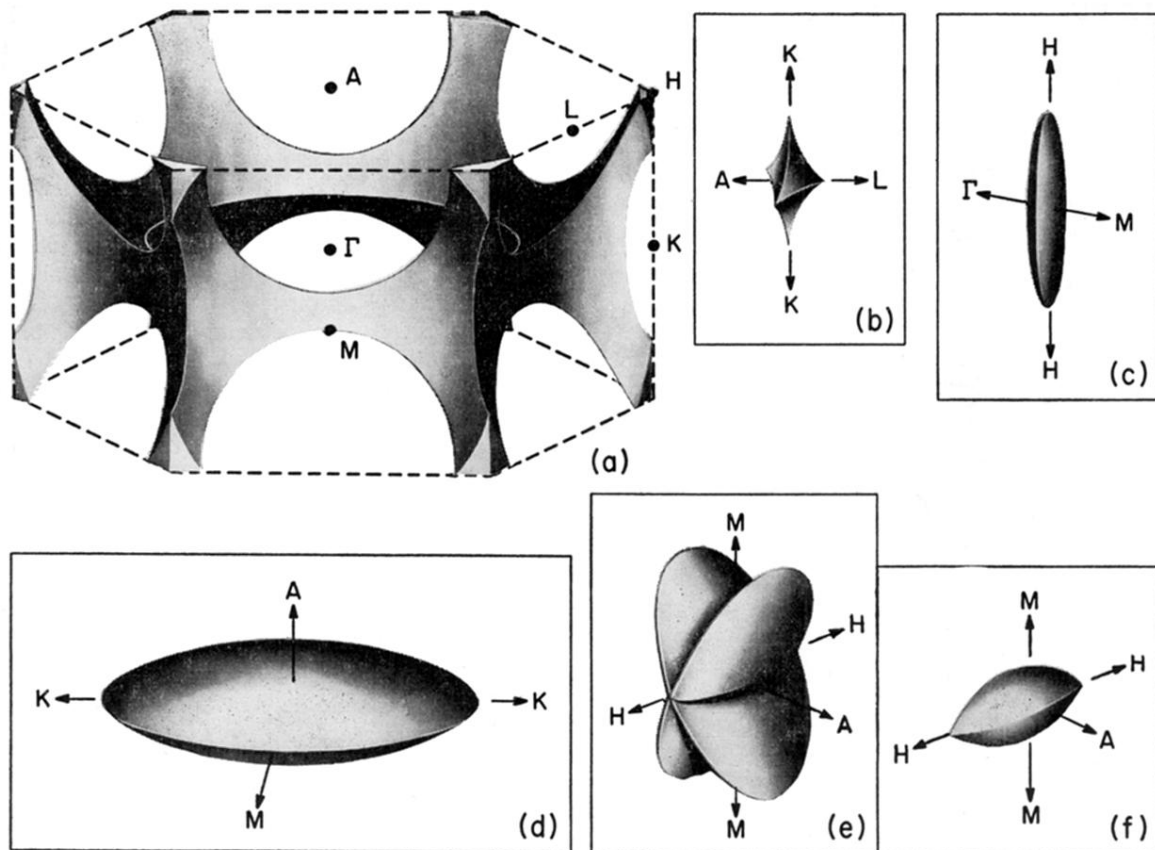
FIG. 3. The single-OPW model Fermi surface for magnesium: (a) monster (2nd-zone holes); (b) cap (1st-zone holes); (c) cigar (3rd-zone electrons); (d) lens (3rd-zone electrons); (e) butterfly (3rd-zone electrons); (f) fourth-zone electrons.